Experimental Characterization and Two-Dimensional Simulation of Short-Crack Propagation in an Austenitic-Ferritic Duplex Steel

O. Düber[1], B. Künkler[2], U. Krupp[1*], H.-J. Christ[1], C.-P. Fritzen[2]

[1]Institut für Werkstofftechnik, Universität Siegen,

[2]Institut für Mechanik und Regelungstechnik - Mechatronik, Universität Siegen,

57068 Siegen, Germany

Abstract

The major part of service life of high-cycle-fatigue-loaded components is determined by crack-initiation and short-crack propagation at loading conditions where no technical crack might be expected. Consequently, microstructural cracks can not be treated by conventional methods of linear-elastic fracture mechanics (LEFM). On the basis of a thorough experimental study of the interactions between microstructural features, like the crystallographic orientation distribution, and the respective crack propagation rate a numerical micro-mechanical crack-propagation model has been developed, which accounts for the abnormal propagation behaviour of short cracks as compared to long cracks in a two-phase austenitic-ferritic duplex steel. In order to simulate real cracking events, the barrier strengths of phase and grain boundaries, beside the orientation of slip planes the most important input parameters for the model, were determined by means of a Hall-Petch analysis using cyclic stress-strain data of single-phase austenitic and ferritic steels as well as of the duplex steel.

Keywords

short crack propagation, duplex steel, EBSD, modelling, fatigue-life prediction

* corresponding author: e-mail: krupp@ifwt.mb.uni-siegen.de, phone: +49 271 7402184, fax: +49 271 7402545

1. Introduction

Generally, the fatigue damage process can be subdivided into three phases: (i) crack initiation, (ii) short-crack propagation, and (iii) long-crack propagation. Conventional fatigue-life prediction methods do either not separate between the individual stages (total-life approach, based on *S-N* curves) or do only take long-crack propagation into account (damage-tolerant approach). The latter is based on the characteristic sigmoidal shape of the *da/dN* vs. ΔK curve (see Fig. 1), the slope of which can be given by empirical power laws according to Paris and Erdogan [1] or McEvily [2].

Fig. 1

However, in many cases, e.g., smooth components loaded in the high-cycle fatigue regime, more than 90% of service lifetime lies within the first two phases of the damage process, i.e., within stage I according to Fig. 1 [3]. Short crack initiation can occur at loading conditions far below the threshold range of the stress intensity factor for technical cracks ΔK_{th} as a consequence of local strain concentrators such as pores, inclusions, surface roughness, or the elastic anisotropy of grains and/or second phases [4-6]. Once initiated, short-crack propagation is significantly affected by local microstructural features. Depending on the crystallographic orientation, cracks may grow along individual slip bands, by alternating operating slip systems governed by the applied normal stress or in an intercrystalline manner along weak interfaces.

Grain or phase boundaries act as microstructural obstacles to short crack propagation, the strength of which varying with the crystallographic orientation relationship [7,8]. The higher the tilt and twist misorientation angle between adjacent slip bands the more effective acts the grain boundary as a barrier to the transmission of the plastic deformation into the neighbouring grain [5,9,10]. This mechanism, which is responsible for the abnormal growth behaviour of microstructurally short cracks, is the theoretical backbone of the analytical short-crack models of Taira et al. [11] and Navarro and de

los Rios [12]. A dislocation pile-up between the advancing crack tip and the grain boundaries gives rise to a decrease in the crack propagation rate *da/dN* and an increase of the elastic stress acting on a dislocation source in the adjacent grains. Once a critical stress is exceeded, the source becomes activated extending the plastic zone ahead of the crack tip into the respective grain, and hence, resulting in a sudden increase in *da/dN* (see Fig. 1). The models have been extended and modified by numerous studies, e.g., to take the distribution of crystallographic orientations into consideration [13], or to account for work hardening on the activated slip planes [14].

Recently, a numerical model has been developed, in which the dislocation pile-up ahead of the crack tip is treated by a boundary-element approach. This model is capable to handle two-dimensional and multi-phase microstructures with given geometries and crystallographic orientations of the grains, based on experimental results obtained by automated electron back-scattered diffraction (EBSD). In the present study the model, which is introduced and described in section 5, was applied to an austenitic-ferritic duplex steel, where local short-crack propagation rates strongly vary depending on the present phase area and boundary type. Hence, earlier results on the significantly different contribution of the austenite phase and the ferrite phase to the overall deformation and damage process, e.g., by Johannson and Óden [15], Llanes et al. [16], and Stolarz [17], can be quantitatively discussed in order to contribute to improved methods of mechanism-oriented life prediction.

2. Materials and experimental details

The experiments were carried out using the austenitic-ferritic duplex stainless steel X2CrNiMoN 22 5 3 (1.4462). Because of their high strength compared to conventional austenitic steels and their excellent corrosion resistance, duplex steels are often used in the chemical industry or for off-shore components, e.g., shafts in boats or wind-power plants. In the as-received condition, it has a very fine, lamellar microstructure, resulting

from the rolling process, with an average grain size of about d=10 μm and an α/γ-volume ratio of approximately 0.5. Its chemical composition is given in Table 1. The microstructure was coarsened by heat treatment in order to simplify microcrack observations (resulting grain size: d_α=50μm, d_γ=35μm). The determination of the barrier strength of the different types of boundaries was done by a Hall-Petch analysis. The Hall-Petch analysis required a variation of the grain size of the material. Therefore, the as-received material was heat treated at 1250°C for 1, 2 and 4 h and water-quenched. In addition to the duplex steel, a ferritic steel (1.4511) and an austenitic steel (1.4404) with similar chemical composition as the respective phases in the duplex steel were studied as single-phase reference materials. Their chemical composition is shown in Table 1, as well.

Table 1

The quantification of the barrier strength of the boundaries required the determination of the cyclic stress-strain curve (CSSC) for the single-phase austenite and ferrite and the two-phase duplex steel. For this purpose, incremental step tests (IST) were performed in a servohydraulic testing system (MTS810) under plastic-strain control and a constant plastic-strain rate of $\dot{\varepsilon}_{pl} = 5 \cdot 10^{-4}\,\mathrm{s}^{-1}$ with specimens having different grain sizes. The stress response of the saturation hysteresis loop of the IST was used to generate the respective CSSC, which led to the cyclic yield stresses σ_{Yc} of the three steels.

Push-pull fatigue tests for microcrack characterization were carried out under stress control using cylindrical, shallow-notched specimens according to Fig. 2. This geometry ensures that cracks initiate in a limited, approximately flat area within the gage length.

Fig. 2

The tests were done with a load-ratio of R=-1 and a frequency of f=1 Hz. After certain numbers of cycles the specimens were periodically removed from the testing machine

and the shallow-notch areas were examined in a scanning electron microscope (SEM Phillips XL 30) using electron channeling contrast and automated EBSD (TSL OIM™) to evaluate microcrack lengths and the crystallographic orientations of the grains involved, respectively. For the EBSD investigations, a very smooth and disruption-free specimen surface is required. Therefore, the specimens were ground and electropolished for 15-30 min at 12°C in an electrolyte consisting of 8 vol.% perchloric acid (70%), 70 vol.% ethanol, 10 vol. % diethylene glycol monobutyl ether, and 12 vol.% distilled water.

The EBSD technique was also used for the determination of the stereological parameters that were necessary for the Hall-Petch analysis. They can be obtained by applying the line sectioning method to metallographic samples of the respective materials. In case of the single-phase austenitic and ferritic steel, these samples were achieved by conventional etching methods. For the two-phase duplex steel the problem arose, that one could not distinguish between phase and grain boundaries. Therefore, the EBSD technique was applied to electropolished sections of the duplex steel which made all different kinds of boundaries visible.

3. Results

3.1 Microcrack propagation

Resulting from the interrupted fatigue tests it turned out, that crack propagation in the short-crack regime followed two different propagation mechanisms, which were termed single-slip and double-slip crack propagation. The single-slip mechanism corresponds to stage I-crack growth and takes place on exclusively one slip system. It results in straight crack paths which follow a slip plane with a high Schmid factor. In the double-slip mechanism the crack path is assembled from two alternating operated slip systems, which is similar to the Neumann description of stage II-crack growth [18]. In this case,

the crack path deflects towards a direction which is more or less perpendicular to the applied stress axis.

The activated slip planes were identified by measuring the crystallographic orientations of the respective grains. With these orientation data it was possible to calculate the trace angles between the operated slip planes and the specimen surface in given grains. By comparing measured trace angles on the specimen surface with calculated trace angles, the activated slip planes could be identified. For the double-slip mechanism, the combination of two slip planes by means of vector algebra yields the resulting crack plane, which - again in combination with orientation data - revealed the trace angle of the new crack plane in a given grain. The respective vector additions are represented schematically in Fig. 3.

Fig. 3

Fig. 3 shows two simplified fcc unit cells. Each of them contains one {111}-type slip plane: a (111) plane in the upper cell and a $(11\bar{1})$ plane in the lower cell. The new crack front for a crack grown in double slip corresponds to the intersecting line of both planes $\vec{s} = [1\bar{1}0]$. The new crack growth direction for such a crack is a linear combination of four slip directions on the two {111}-type planes (dashed lines in Fig. 3): the effective Burgers vector for the upper plane can be calculated according to $\vec{b}_{1eff} = [\bar{1}01] + [0\bar{1}1] = [\bar{1}\bar{1}2]$ and for the lower plane according to $\vec{b}_{2eff} = [\bar{1}0\bar{1}] + [0\bar{1}\bar{1}] = [\bar{1}\bar{1}\bar{2}]$. These two partial effective Burgers vectors can be added to the effective Burgers vector $\vec{b}_{eff} = \vec{b}_{1eff} + \vec{b}_{2eff} = [\bar{1}\bar{1}0]$, which is the new crack-growth direction. Finally, by computing the cross product of the new crack front and the new crack-growth direction, the new crack plane is obtained as: $\vec{s} \times \vec{b}_{eff} = (001)$.

Now, the trace angle of the new crack plane can be calculated and compared with measured trace angles.

Examples are given in Fig. 4: Fig. 4a shows a short crack that has initiated at an α/γ-phase boundary. Between ① and ② the crack has grown in single slip on the denoted slip planes, while between ② and ③ crack growth was operated by double slip alternating on (111) and $(\bar{1}11)$ planes. The double-slip part is approximately perpendicular to the loading direction. By following the calculation explained above, consideration of the two involved slip planes in equal parts would lead to a new (100) crack plane and a trace angle of about 20°. This calculated trace angle would not match the measured trace angle of about 0°. If the contribution of the (111) plane to the crack growth is twice as high as the contribution from the $(11\bar{1})$ plane, the new crack plane would be a (311) plane with a trace angle of –1° in the respective grain, which is in good agreement with the measured trace angle.

Fig. 4a,b

Fig. 4b shows a second example. The path of this crack can also be subdivided into parts that have grown in single slip on the indicated slip planes and a part that has grown in double slip under participation of a (111) plane and a $(\bar{1}11)$ plane. Again, the measured trace angles could be calculated by vector addition of slip increments on the participating slip planes.

Another phenomenon, which becomes evident from Fig. 4b is the ability of the crack to return to single-slip propagation after it has grown by the double-slip mechanism. This will be discussed in section 5.

A substantial difference in the crack growth rates was found for the single-slip and the double-slip mechanism. From Fig. 5a (which shows the same crack than Fig. 4b) it is evident, that crack propagation in single slip is faster than in double slip. The vertical lines indicate the crack tip advance after identical intervals of 10,000 cycles. Fig. 5b shows another example. Here, the vertical lines show how the crack tip position has

changed after intervals of 30,000 cycles. When the left crack tip approaches a twin boundary it is blocked and almost stopped. By applying 5,000 overload-cycles (with an increase in the loading amplitude from $\Delta\sigma/2$=350 MPa to 450 MPa) the crack-growth rate increased dramatically (the distance between the dashed lines shows the crack advance after 5,000 cycles) and the crack could be forced to continue its growth over this boundary. In the following grain the crack starts to grow in double slip. After reducing the amplitude, the growth rate dropped immediately but stayed well above zero.

The grain boundary between the grains α_1 and α_2 has no significant influence, neither on the crack growth rate nor on the crack path direction, even though there is a misorientation of θ=49° between these grains (Fig. 5c). By successively removing thin layers from a plane parallel to the loading axis (indicated by arrows) the crack path underneath the surface of the two grains was made visible. Fig. 5c shows clearly, that there is only a small twist misorientation angle between these two planes, i.e., for crossing the $\alpha_1\alpha_2$ grain boundary the crack had to overcome only a slight change in the crack plane.

Fig. 5a,b,c

3.2 Quantification of the barrier effect of grain and phase boundaries

Grain and phase boundaries are known to serve as obstacles to dislocation motion/crack propagation. The extent of this blocking effect depends on the nature of the boundary and can be quantified by a Hall-Petch analysis. According to Hall [19] and Petch [20], plastic deformation leads to a pile-up of dislocations in front of a boundary. This pile-up causes stress concentrations at the boundary and in the adjacent grain. When the stress concentration is high enough and reaches a critical value, a dislocation source in the adjacent grain is activated and plastic deformation can spread out into this grain.

The original Hall-Petch relation

$$\sigma_Y = \sigma_Y^0 + k_y \cdot \frac{1}{\sqrt{\overline{d}}} \qquad (1)$$

relates the yield stress of a material to its mean grain size. σ_Y^0 is the friction stress

which is required to overcome the lattice friction, and k_y is the Hall-Petch constant,

which can be seen as a measure for the boundary resistance to dislocation motion. In

this form the equation is valid for single-phase materials and monotonic loading only.

Hence, it has to be extended for multi-phase materials subjected to cyclic loading

conditions.

According to Fan et. al. [21], the extension for multi-phase materials can be done by

combining the contributions of the different types of boundaries to the yield stress.

These contributions are multiplied with weighting factors, so-called stereological

parameters, which describe the geometrical arrangement of the phases in space and thus,

take into account how often a boundary occurs. The extension on cyclic loading was

done by simply replacing the monotonic yield stress by the cyclic yield stress, which

was considered to be reasonable, as long as planar slip prevails leading to dislocation

pile-ups at the boundaries. The resulting equation for the cyclic Hall-Petch constant of

an α/γ-phase boundary is

$$k_{y,cyc}^{\alpha\gamma} = \frac{(k_{y,cyc}^c - k_{y,cyc}^\alpha \cdot f_{\alpha c} - k_{y,cyc}^\gamma \cdot f_{\gamma c})}{F_s} . \qquad (2)$$

All parameters on the right hand side of the equation can be determined experimentally,

while the cyclic Hall-Petch constant for a phase boundary $k_{y,cyc}^{\alpha\gamma}$ has to be calculated.

$k_{y,cyc}^c$, $k_{y,cyc}^\alpha$, and $k_{y,cyc}^\gamma$ are the Hall-Petch parameters of the double-phase duplex steel

and the single-phase ferritic and austenitic steels according to Table 1. $f_{\alpha c}$ and $f_{\gamma c}$ are

the continuous volumes of the respective phases in the duplex steel, and F_s is the degree

of separation of the duplex steel. The three values of $k_{y,cyc}$ were determined by drawing

a Hall-Petch plot which shows the cyclic yield stress against the mean grain size or "cluster size", respectively (Fig. 6). The slope of the curves corresponds to the cyclic Hall-Petch constant. In case of the duplex steel, the mean cluster size substitutes the mean grain size, because not only grain boundaries but also phase boundaries contribute to the yield stress, and therefore, the mean "phase size" has to be taken into account, too. The mean cluster size $\overline{d}_{\alpha\gamma}$ is the mean value of the mean grain sizes for the α and γ grains and the mean phase sizes of the α and γ phase, respectively:

$$\overline{d}_{\alpha\gamma} = (\overline{d}_{\alpha\alpha} + \overline{d}_{\gamma\gamma} + \overline{d}_{\alpha} + \overline{d}_{\gamma})/4.$$

Fig. 6

The stereological parameters were determined by applying the line-sectioning method to microstructure maps from EBSD scans. The continuous volumes $f_{\alpha c}$ and $f_{\gamma c}$ are calculated by multiplying the contiguities C_{α} and C_{γ} with the volume fractions of the two phases in the duplex steel f_{α} and f_{γ}:

$$f_{\alpha c} = C_{\alpha} \cdot f_{\alpha}. \tag{3}$$

The contiguity describes the connectivity of a phase and is calculated according to eq. 4:

$$C_{\alpha} = \frac{2N_{\alpha\alpha}}{2N_{\alpha\alpha} + N_{\alpha\gamma}}, \tag{4}$$

where $N_{\alpha\alpha}$ and $N_{\alpha\gamma}$ are the numbers of intersections of $\alpha\alpha$ and $\alpha\gamma$ boundaries with the random lines from the line-sectioning method. The degree of separation F_{s} describes the volume fraction of isolated grains in the microstructure. It is calculated as the sum of the isolated volume fractions of the phases: $F_{s} = f_{\alpha s} + f_{\gamma s}$ with $f_{\alpha s}$ and $f_{\gamma s}$ as the difference between the volume fraction and the continuous volume of a phase:

$$f_{\alpha s} = f_{\alpha} - f_{\alpha c}. \tag{5}$$

Table 2 shows the experimentally-obtained cyclic Hall-Petch constants for the ferritic ($\alpha\alpha$ GB), the austenitic ($\gamma\gamma$ GB) and the duplex steel with the respective calculated value for the $\alpha\gamma$ phase boundaries. The $\alpha\gamma$ phase boundaries have the highest value for the Hall-Petch constant, which means that these boundaries should exhibit the highest resistance to dislocation motion. The value for the duplex steel is the weighted average of the three types of boundaries. Beside the Hall-Petch constants, the microstructural cyclic yield stresses were obtained, which are the cyclic pendants of the friction stresses of the two phases. It is calculated by extrapolating the curves in Fig. 6 until they intersect with the y-axis.

Table 2

4. Modelling Short Cracks

The model originally designed to simulate short crack propagation in stage I is based on the experimental investigations presented above. In many cases, short cracks propagate on slip planes inclined by an angle of about 45 degrees to the loading axis, resulting in a zigzag-like crack shape (Figs. 4 and 5). Plastic slip deformation on these planes is blocked by grain and phase boundaries (Fig. 5), according to the models of Taira et al. [11] and Navarro and de los Rios [12]. The model describes the crack and its plastic zones by a series of slip band pieces (Fig. 7). Along the slip bands tangential displacements of their two faces relative against each other are possible by dislocation glide. These displacements are modelled by means of mathematical edge dislocations (Hills et al. [22]). The crack is defined as that part of the slip band that is, in addition to the tangential displacements, also allowed to exhibit normal displacements, modelled by a second set of mathematical edge dislocations. Plastic deformation in front of the crack tip occurs if the shear stress on the slip band exceeds a critical value corresponding to the resistance of dislocations against motion. Thus, an elastic perfectly-plastic behaviour of the plastic zone is simulated. The dislocation distribution is calculated

numerically by a boundary element method which assumes a constant displacement inside each element. Each boundary element consists of a negative edge dislocation at the one end and a positive edge dislocation at the other end. This is schematically represented in Fig. 7. To determine the stresses on arbitrary positions around the crack, so-called "sensor elements" are used, which do not represent any displacement.

Fig.7

To formulate the boundary element method, the influence function G^{ij} that describes the stress on the center of an element i resulting from the displacement b^j in an element j has to be calculated. This is performed by superimposing the stress fields of the two or four dislocations representing the tangential or tangential and normal displacement in the slip band element or in the crack element, respectively. The overall stress on the element i results from the summation of the stresses generated by all other elements with the applied normal stress $\sigma_{nn}^{i\infty}$ and the shear stress $\tau_{tn}^{i\infty}$. For p crack elements and q elements within the slip bands ahead of the crack tip a linear system of equations can be established, which has to meet the following boundary conditions in an element-specific coordinate system:

- any normal stress σ_{nn}^i must vanish when the crack is open (Eq. 5) and no negative normal displacements are allowed (Eq. 7),

- the crack faces are free of shear stresses ($\tau_{tn}^i = 0$, no friction), and

- within the plastic zones ahead of the crack tip the shear stress τ must not exceed the resistance τ_b to dislocation motion (Eq. 6, assumed as to be equal to the microstructural cyclic yield stresses as derived in section 3).

These conditions lead to a linear system of inequalities that yields the displacements of all elements in normal direction b_n^i and tangential direction b_t^i and thus the crack tip

slide displacement *CTSD*. By allowing only positive normal displacements within the crack elements, geometrical crack closure can be taken into account (Eq. 7).

$$\sigma_{nn}^i = \sum_{j=1}^{p} G_{nn,n}^{ij} b_n^j + \sum_{j=1}^{p+q} G_{nn,t}^{ij} b_t^j + \sigma_{nn}^{i\infty} \qquad \leq 0 \qquad i=1...p,$$ (5)

$$\left| \tau_{tn}^i \right| = \left| \sum_{j=1}^{p} G_{tn,n}^{ij} b_n^j + \sum_{j=1}^{p+q} G_{tn,t}^{ij} b_t^j + \tau_{tn}^{i\infty} \right| \qquad \begin{cases} = 0 & i=1...p \\ \leq \tau_b & i=p+1...p+q \end{cases}$$ (6)

$$b_n \qquad \geq 0 \qquad\qquad\qquad\qquad i=1...p.$$ (7)

The crack propagation rate *da/dN* is calculated from the range of the crack tip slide displacement Δ*CTSD* (obtained by a cyclic calculation of the system of inequalities) by means of the power law function

$$\frac{da}{dN} = C \cdot \Delta CTSD^m.$$ (8)

C is a material-specific constant and *m* is an exponent (mostly equal to one). The crack tip opening displacement *CTOD* is zero because the model does not allow normal displacements in the plastic zone. Therefore, crack growth operates only by slide displacement on slip bands parallel to the crack plane. According to Wilkinson and Roberts [23], eq. 8 is based on the idea that plastic sliding due to external loads causes dislocation emission at the crack tip and that during reverse loading dislocations of opposite sign are emitted. Hence, vacancies are produced leading to crack advance. For a more detailed description of the model, see Schick [24] and Krupp et al. [5].

The barrier effect of grain and phase boundaries, as described in section 3, leads to a deceleration of the crack due to a dislocation pile-up at the boundary until a dislocation source in the neighbouring grain is activated. This is simulated by adding sensor elements in the neighbouring grains representing the possible slip systems, depending on the orientation of the individual grains (Fig. 8a). With increasing crack length, the shear stress on these sensor elements increases. If a boundary-dependent critical stress

value τ_{crit} is reached, the corresponding slip band is meshed and plastic deformation can propagate across the boundary (Fig. 8b). The value of

$$\tau_{\text{crit}} = \frac{k_{y,cyc}}{2M_S\sqrt{r}} \, , \tag{9}$$

depends on the value of $k_{y,cyc}$, which is the Hall-Petch coefficient of the respective boundary (see section 3). M_S is the Schmid factor and r is the distance between the centre of the sensor element and the boundary. After propagation of slip through the boundary, the dislocation pile-up is vanished and thus, the crack growth rate increases until the next boundary is reached resulting in a new dislocation pile-up.

Fig. 8a,b

As it can be derived from section 3, crack propagation takes place on single slip planes in stage I only for a few grains. Then, the propagation mechanism changes to crack propagation on multiple slip systems. In order to determine the point of transition, a ring of sensor elements was placed at the tip of an inclined crack (Fig. 9a). These sensor elements were used to calculate the elastic stress field (grey curve in Fig. 9b) and the linear elastic perfectly-plastic stress field with plastic deformation on one slip plane only (black curve in Fig. 9b) around the crack tip in a constant radius.

Fig. 9a,b

The stress distribution for the elastic crack calculated by the boundary-element model is identical to the analytical solution. However, the stress distribution for the elastic perfectly-plastic crack exhibits a decrease of the shear stress near the slip plane until the plastic shear stress τ_b is reached. In a larger distance from plastic deformation, the shear stress is nearly as high as for the elastic crack.

In Fig. 10a, additional sensor elements representing further slip planes of the grain are positioned at the crack tip to determine the shear stress on these planes. As soon as a critical stress value is exceeded at one of these sensor elements, the respective slip plane

is considered to become "activated" and plastic deformation occurs on this second slip plane (Fig. 10b). This is in accordance to Lin and Thomson [25], stating that a certain stress intensity has to be reached to activate additional slip systems in front of an advancing crack tip. This happens only above a certain crack length, because the elastic shear stress increases with crack length. Accordingly, the shear stress in the elastic-plastic calculation outside the plastic zone increases. After the activation of the second slip plane, the new crack tip position results from the contributions of the plastic slip vectors (Fig. 10c). The calculation of the plastic slip vectors is analogous to the calculation of $\Delta CTSD$, where plastic deformation only occurs if the shear stress τ exceeds the resistance τ_b against dislocation motion. New sensor elements are now positioned at the new crack tip, representing new slip planes and again these elements are activated. Hence, with growing crack length, the crack becomes deflected onto a path perpendicular to the loading axis (stage II, long cracks, Fig. 10d). If the orientations of the slip planes change (because the crack tip has reached a new grain) and the crack is still relatively short, crack propagation can return to the single-slip mechanism because no adequate second slip plane is available. This is in accordance with our experimental observations.

Fig. 10

The proposed model can also be used to simulate two-dimensional short crack propagation in virtual microstructures, generated by the Voronoi algorithm (Voronoi [26]). These microstructures have a statistical grain size and crystallographic orientation distribution that can be adjusted to the results of the EBSD orientation measurements. Simulations were performed for stage I crack propagation in a duplex steel to estimate the influence of the microstructural arrangement as described by stereological parameters on short crack growth (Künkler et al. [27]). Furthermore the influence of varying loading amplitudes on $\Delta CTSD$ can be considered (Schick [24]).

5. Verification and discussion

In order to verify the crack propagation model, it was applied to crack geometries observed during fatigue experiments. The starter cracks were defined in the model according to the ones obtained in the experiments before they were subjected to cyclic loading calculations. As an example, Fig. 11 shows the simulated crack length versus number of loading cycles in comparison with experimental data for two short cracks in duplex steel.

Fig. 11a,b

The observed deceleration of the left-hand crack tip in Fig. 11a can be explained by a dislocation pile-up at the phase boundary. This behaviour was reproduced by the simulations. In Fig. 11b, the calculated crack-growth rates in stage I of the left-hand and right-hand crack tip also fit the experimental data. The difference in the calculated crack growth rates of the two tips is mainly due to the difference in the resistance against shear deformation in the individual phases and due to the difference in the shear stresses acting on the crack planes, which depend on the orientation of the crack paths with respect to the loading axis. This has a strong impact on the crack tip slide displacement range $\Delta CTSD$ and hence the crack growth rate. Therefore, the proposed model is able to represent the effect of different kinds of microstructural barriers and different phases on stage I crack propagation in a mechanism-oriented way.

To verify the simulation of crack propagation operating by a double-slip mechanism, experimentally observed cracks growing by alternating operated slip planes were defined in the model (Fig. 12, which shows the upper left corner of the crack in Fig. 5b after 10^6 cycles) using the geometry and crystallographic orientation of the respective grains. The value for the shear stress τ_b is the same as for the simulations of stage I cracks. The length of the additionally activated slip planes is restricted by the grain

boundaries. The diagram in Fig. 12 shows the simulated crack length versus number of loading cycles in comparison with experimental data.

Fig. 12

As mentioned in section 3, the left crack tip in Fig. 5b almost stopped in front of a boundary. By applying overloads, the blocked crack abruptly accelerated, grew over this boundary and entered the next grain, where crack advance took place in double slip. After reducing the loading level to the one before, the growth rate dropped immediately but stayed above zero. This can presumably be attributed to the fact, that the crack is already relatively long and therefore is not longer a stage I-crack. Also the favourable orientation of the slip planes involved can play a role in this context. In the model, the acceleration of the crack growth rate during the overloads could be simulated, but not as high as observed in the experiment. The crack propagation rate after the overloads could be reproduced by the model (Fig. 12) with the same value for the constant *C* as for short-crack growth in single slip (Fig. 11b). Also the calculated crack path is in accordance with the experimentally observed one. Thus, the model seems to be able to simulate crack propagation on multiple slip planes in a mechanism-oriented way.

6. Conclusions

By interrupted fatigue experiments it could be shown that crack propagation in the short crack regime can be subdivided into two basic mechanisms: operating either by single-slip (crystallographic propagation) and double-slip (propagation perependicular to laoding axis), giving rise to substantially different propagation rates. Additionally, it was found that a crack which has grown in double slip can change to the single-slip mechanism again when entering a new grain that exhibits a slip plane with a low misorientation angle to the crack path.

The barrier strength of grain and phase boundaries to dislocation motion was derived by means of an extension of the classical Hall-Petch relationship. It was shown that in the

studied duplex steel phase boundaries are much stronger obstacles to dislocation motion than grain boundaries in the respective phases.

The model introduced in this paper is capable to simulate two-dimensional short-crack propagation on single slip planes (stage I) and multiple slip planes, taking geometrical crack closure into consideration. The comparison between experimentally-observed and simulated cracks demonstrated a good agreement with respect to the crack lengths as a function of the number of loading cycles. Due to the simple formulation of the boundary element method the model can calculate several thousand cycles in a relatively short time.

References

[1]   Paris PC, Erdogan F. A critical analysis of crack propagation laws. Transactions ASME 1963; 85: 528.

[2]   McEvily AJ. On closure in fatigue crack growth. ASTM STP 982 1988, p. 35.

[3]   Tokaji K, Takafiji S, Ohya K, Kato Y, Mori K. Fatigue behavior of beta Ti-22V-4Al alloy Subjected to surface-microstructural modification. J. of Mater. Sci. 2003; 38: 1153.

[4]   Pearson S. Initiation of fatigue cracks in commercial aluminum alloys and the subsequent propagation of very short cracks. Engng. Fract. Mech., 1975; 7: 235.

[5]   Krupp U, Floer W, Lei J, Hu YM, Christ H-J, Schick A, Fritzen C-P. Mechanisms of short-fatigue-crack initiation and propagation in a ß-Ti alloy. Phil. Mag. A, 2002; 82: 3321.

[6]   Heinz A, Neumann P. Crack initiation during high cycle fatigue of an austenitic steel. Acta Met. Mat. 1990; 38: 1933.

[7]   Zhang YH, Edwards L. On the blocking effect of grain boundaries on small crystallographic fatigue crack growth. Mater. Sci. and Engng. 1994; A188: 121

[8]   Krupp U, Düber O, Christ H-J, Künkler B, Schick A, Fritzen C-P. Application of the EBSD technique to describe the initiation and growth behaviour of microstructurally short fatigue cracks in a duplex steel. J. Microscopy 2004; 213: 313-320.

[9]   Zhang ZF, Wang ZG. Fatigue-cracking characteristics of a copper bicrystal when slip bands transfer through the grain boundary. Mater. Sci. and Engng. 2003; A343: 308.

[10]   Zhai T, Wilkinson A.J. Martin JW. A crystallographic mechanism for fatigue crack propagation through grain boundaries. Acta Mater. 2000; 48: 4917.

[11]   Taira S, Tanaka K, Nakai Y. A model crack-tip slip band blocked by grain boundary. Mec. Res. Comm. 1978; 5(6): 375.

[12]   Navarro A, de Los Rios ER. Short and long fatigue crack growth: a unified model. Phil. Mag. A 1988; 57: 15.

[13]   Wilkinson AJ. Modelling the effects of texture on the statistics of stage I fatigue crack growth. Phil. Mag. A 2001; 81: 841.

[14]   Xin XJ, de los Rios ER, Navarro A. Modelling strain hardening at short fatigue cracks. Proc. Short Fatigue Cracks, ESIS 13, Miller KJ, de los Rios ER, editors, Mechanical Engineering Publications, London, 1992, p. 369.

[15]   Johansson J, Odén M. Load sharing between austenite and ferrite in a duplex stainless steel during cyclic loading. Met. Mat. Trans. 1999; 31A: 1557

[16]   Mateo A, Llanes L, Akdut N, Stolarz J. Anisotropy effects on the fatigue behavior of rolled duplex stainless steels. Int. J. Fatigue 2003; 25: 481.

[17] Stolarz J, Focht J. Specific features of two phase alloy response to cyclic deformation. Mater. Sci. and Engng. 2001; 319-321: 501.

[18] Neumann P. New experiments concerning the slip processes at propagating fatigue cracks-I. Acta Metall. 1974; 22: 1155

[19] Hall EO. The deformation and aging of mild steel: II characteristics of the Lüders deformation. Proc. Phys. Society London B 1951; 64: 747

[20] Petch NJ. The cleavage strenght of polycrystals. Iron Steel Inst. B 1953; 174: 25

[21] Fan Z, Tsakiropoulos P, Smith PA, Miodownik AP. Extension of the Hall-Petch relation to two-ductile-phase alloys. Phil. Mag. A 1993: 67: 515-531

[22] Hills DA, Kelly PA, Dai DN., Korsunsky A.M. Solution of crack problems. London: Kluwer Academic Publishers, 1995.

[23] Wilkinson AJ, Roberts SG. A dislocation model for the two critical stress intensities required for threshold fatigue crack propagation. Script. Mat. 1996; 35: 1365-1371.

[24] Schick A. Ein neues Modell zur mechanismenorientierten Simulation der mikrostrukturbestimmten Kurzrissausbreitung. Doctoral thesis, University of Siegen, 2004.

[25] Lin IH, Thomson R. Cleavage, dislocation emission and shielding for cracks under general loading. Acta Metall. 1986; 34: 187-206.

[26] Voronoi GF. Nouvelles applications des parametres continus a la theorie des formes quadratiques. Zeitschrift für Reine Angewandte Math. 1908; 134: 198-287.

[28] Künkler B., Schick A., Fritzen C-P, Floer W., Krupp U., Christ H-J. Simulation of microstructurally controlled short crack propagation. Steel Research 2003; 74: 514-518.

Table 1: Chemical composition of the steels used in this study (wt.%)

	Fe	Cr	Ni	Mo	Mn	Si	Nb	N	C
1.4462	bal.	21,9	5,6	3,1	1,8	0,5	-	0,1871	0,020
1.4404	bal.	16,6	11,1	-	1,3	0,6	0,01	0,0296	0,018
1.4511	bal.	16,3	-	-	0,7	0,5	0,253	-	0,012

Table 2: Results of the Hall-Petch experiments

	γγ	αα	αγ	Duplex
microstructural cyclic yield stress $\sigma_{b,\,cyc}$ [MPa]	137	198	--	196
cyclic Hall-Petch constant $k_{y,cyc}$ [MPa$\sqrt{\text{mm}}$]	4.2	5.0	15.8	10.1

log *da/dN*

STAGE I   STAGE II   FRACTURE

long-crack propagation K_c

short crack propagation
(according to Navarro & de los Rios [12])

microstructural barriers

(according to Paris & Erdogan [1]):

$$\frac{da}{dN} = C\Delta K^n$$

(according to McEvily [2]):

$$\frac{da}{dN} = C\left(\Delta K - \Delta K_{th}\right)^2 \frac{\Delta K}{K_c - K_{max}}$$

ΔK_{th} $\log\Delta K$
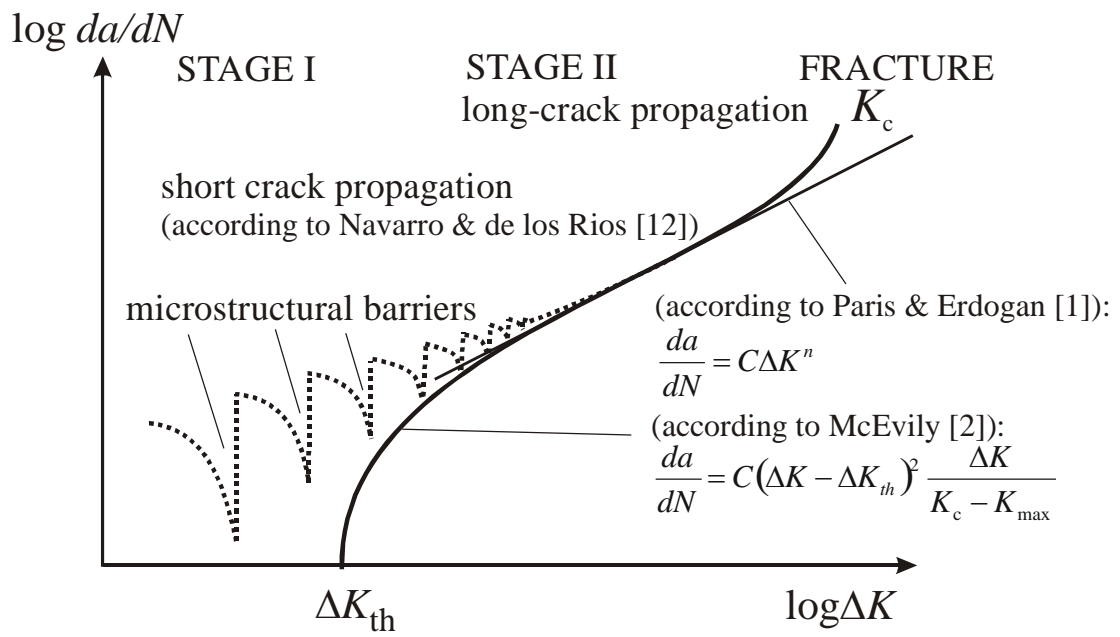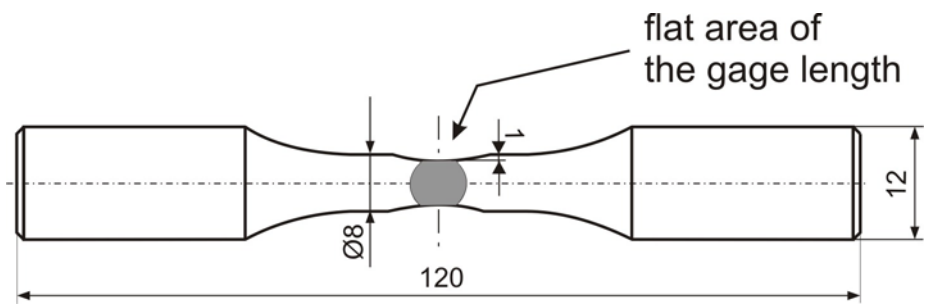
Fig. 1

Fig. 2
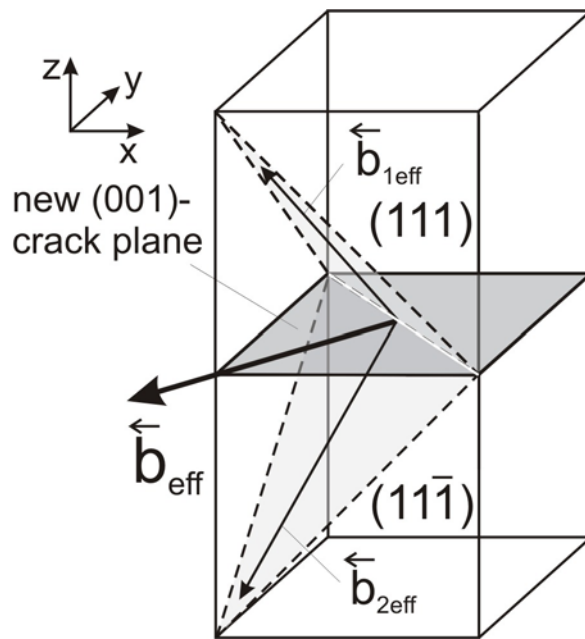
Fig. 3
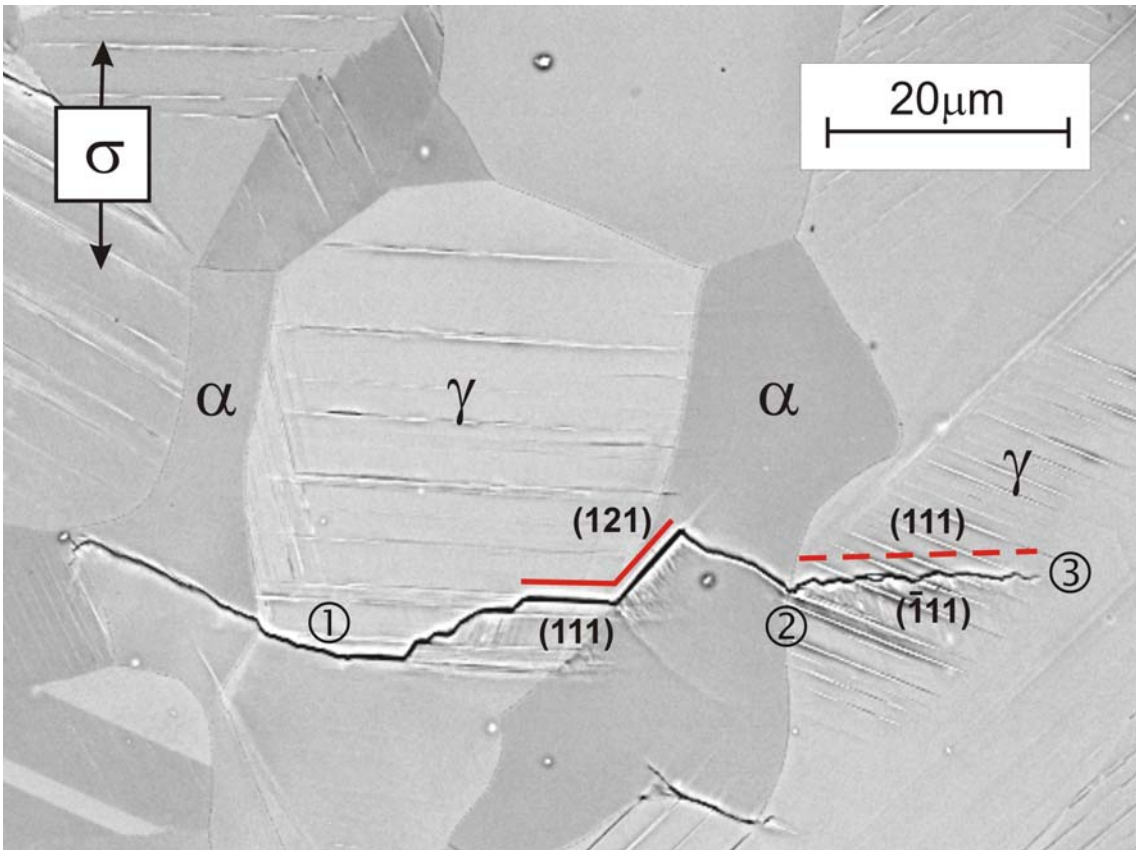
Fig. 4a
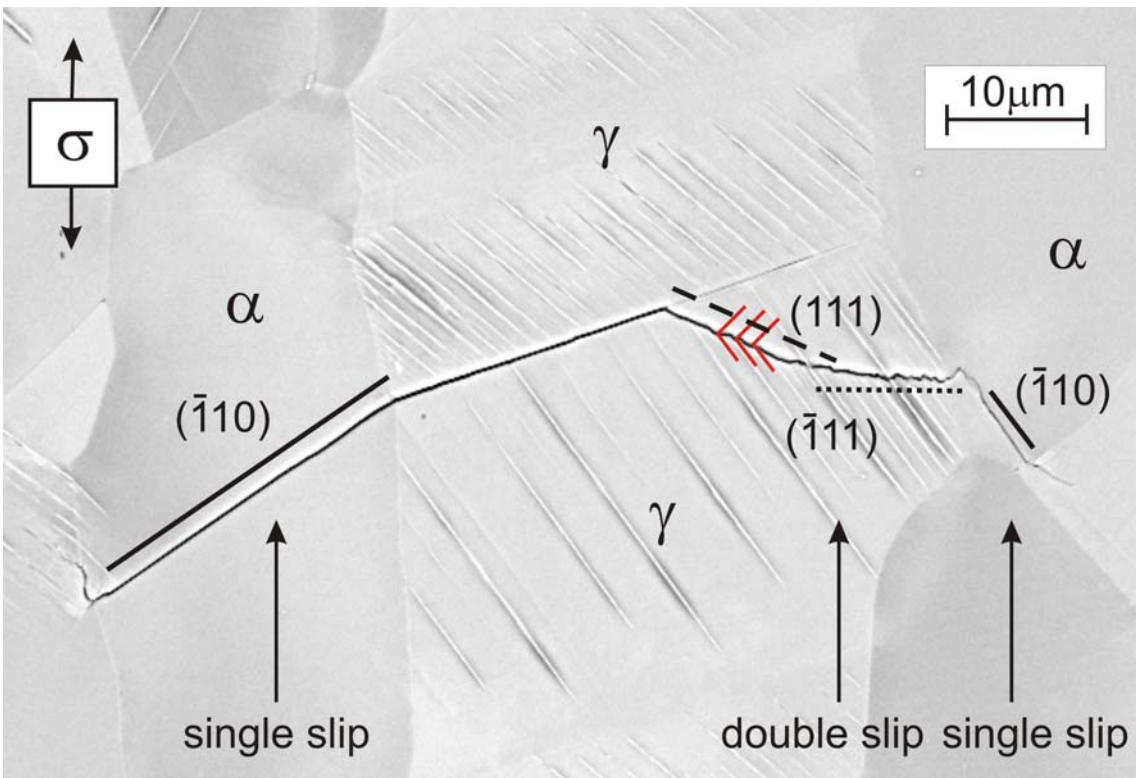
Fig. 4b
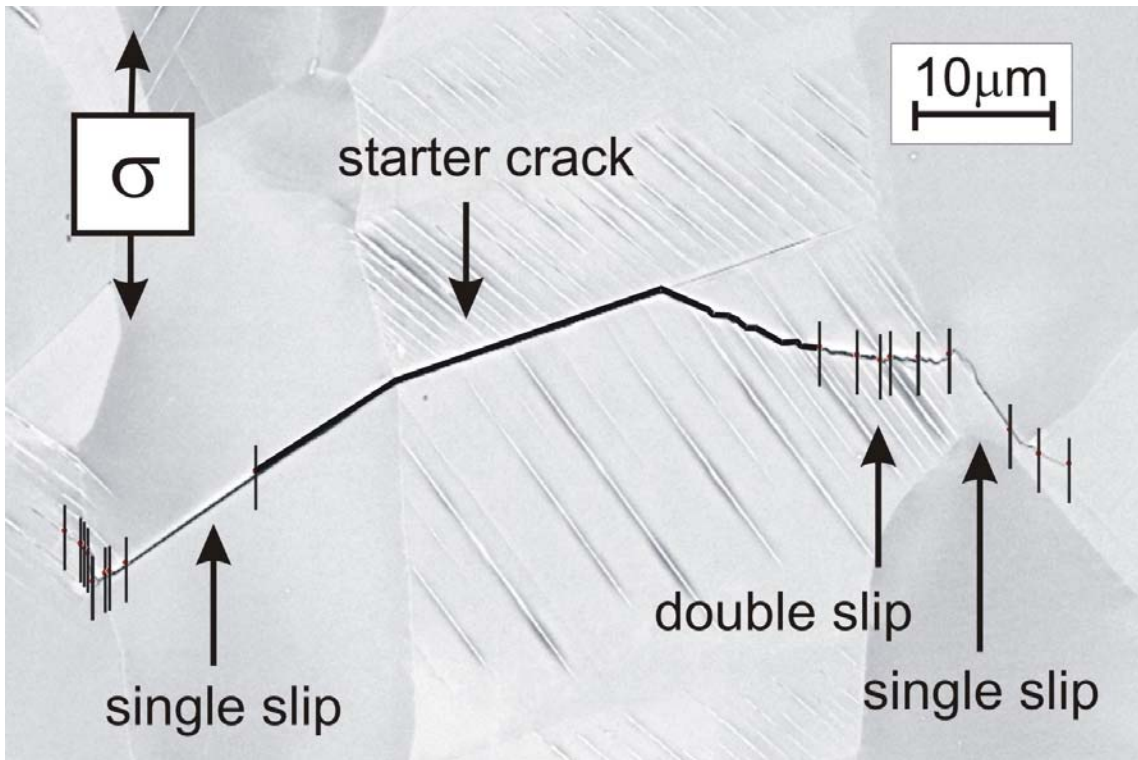
Fig. 5a
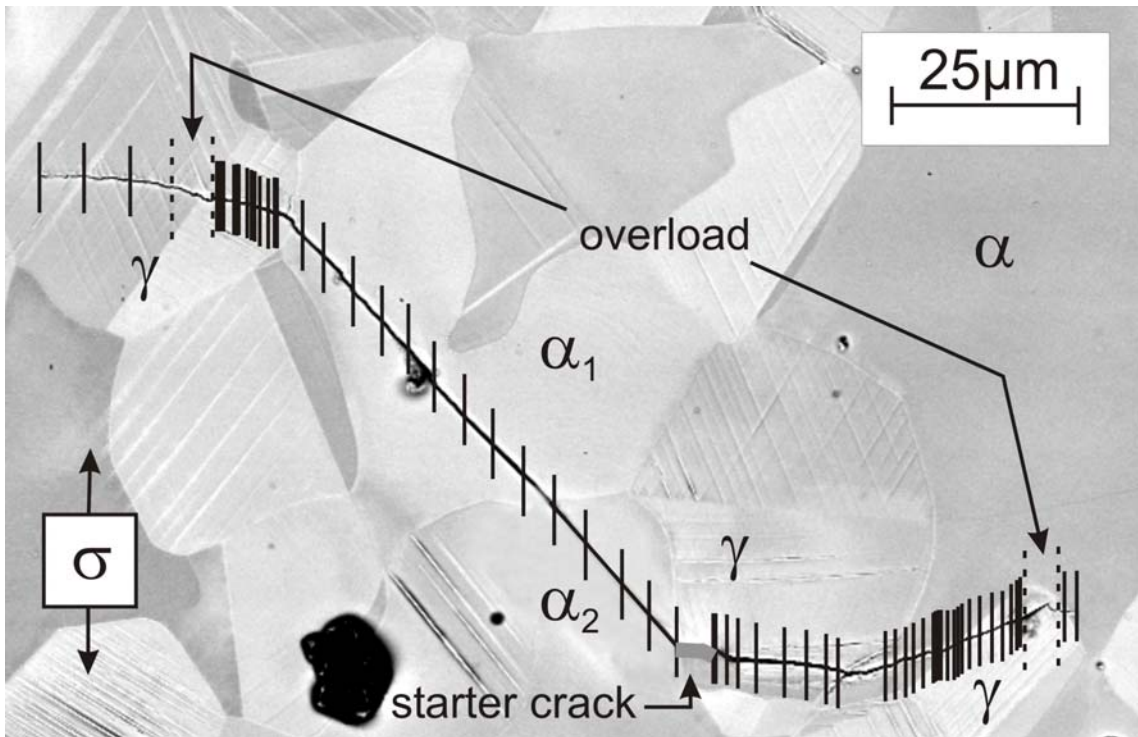
Fig. 5b
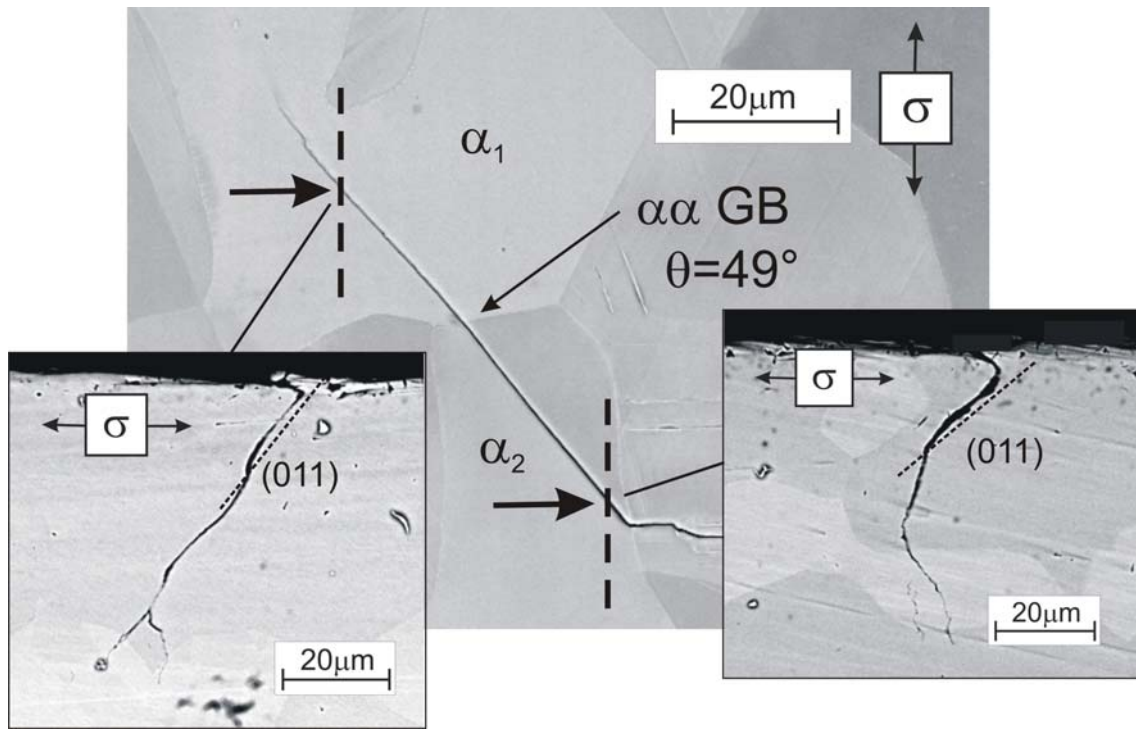
Fig. 5c

Fig. 6

Fig.7

Fig. 8

a)

b)
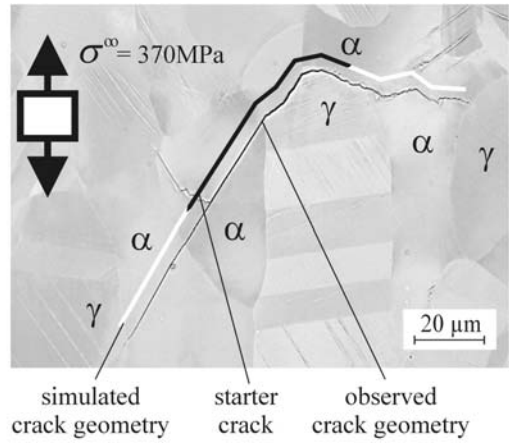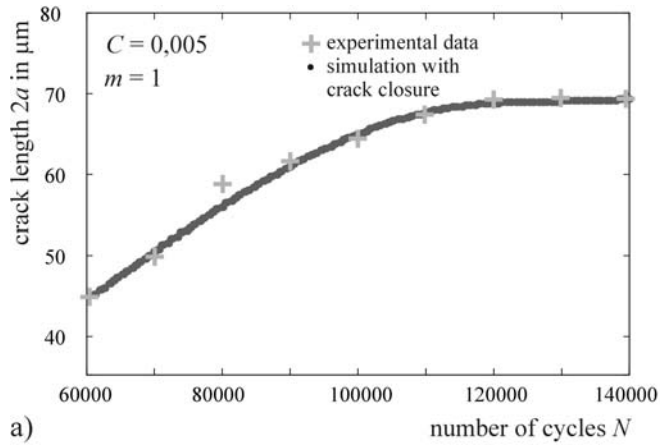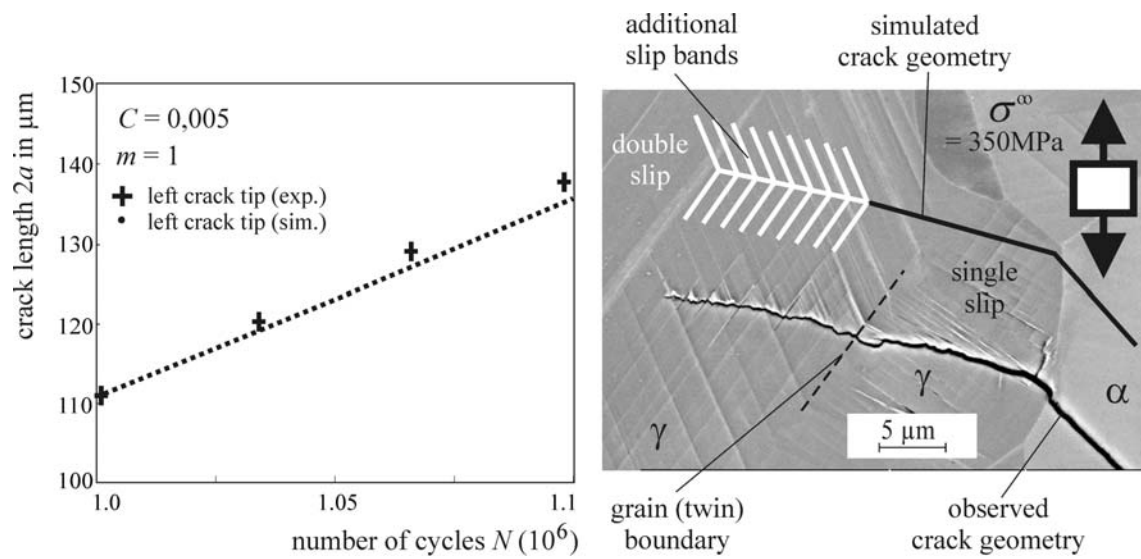
Fig. 9

Fig. 10

a)

b)
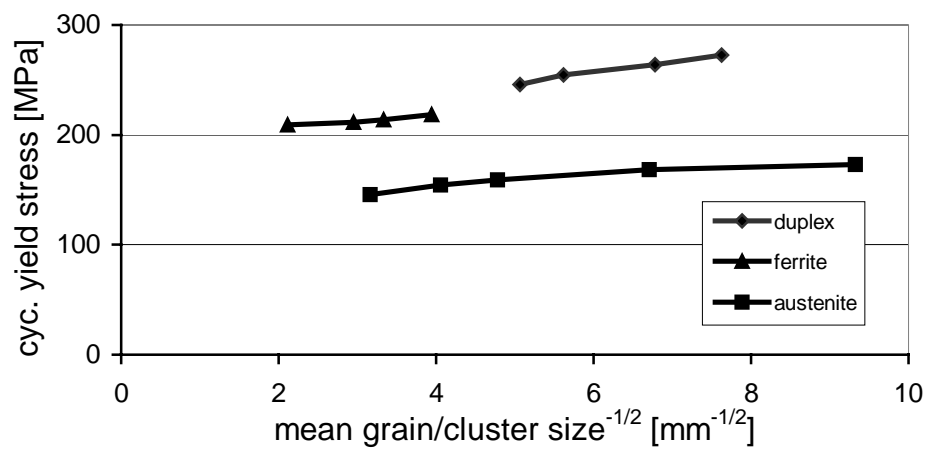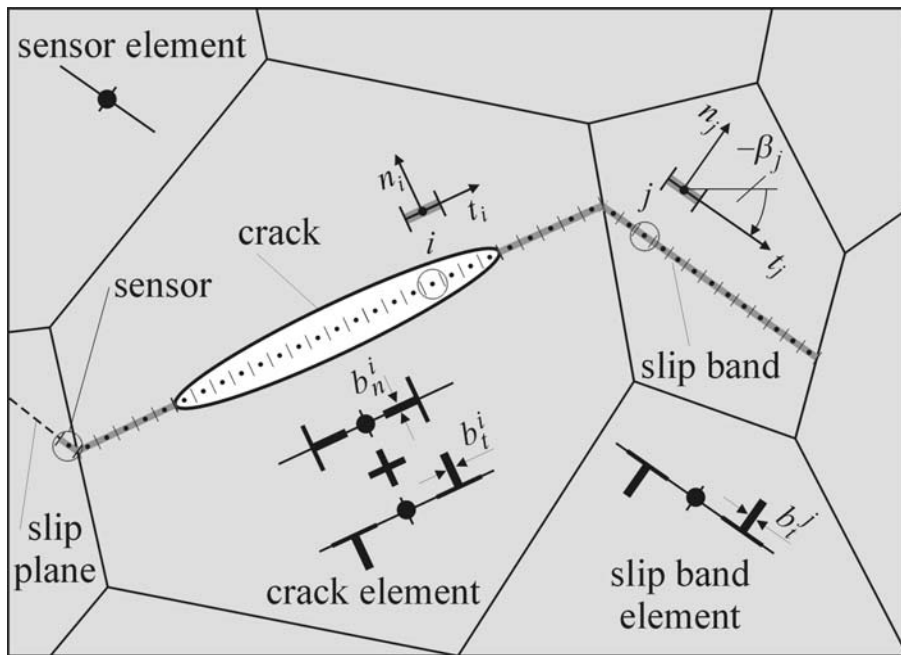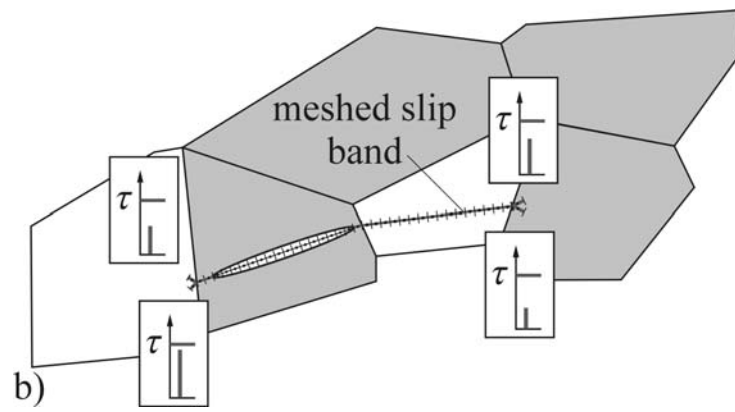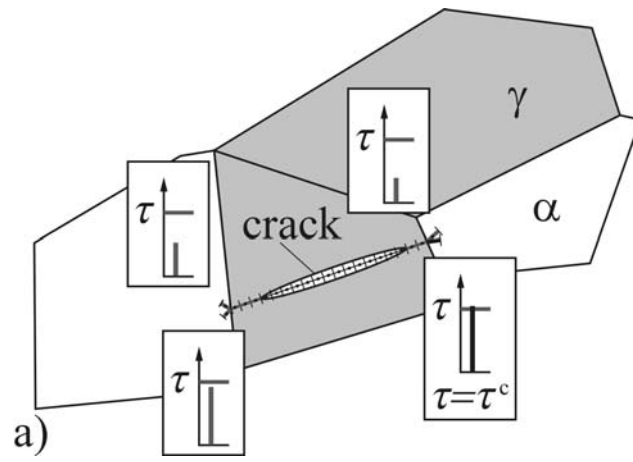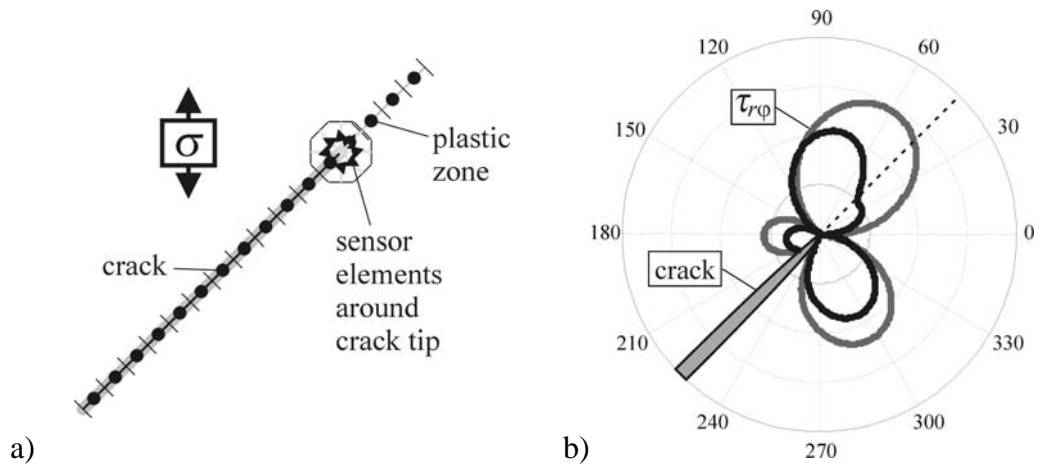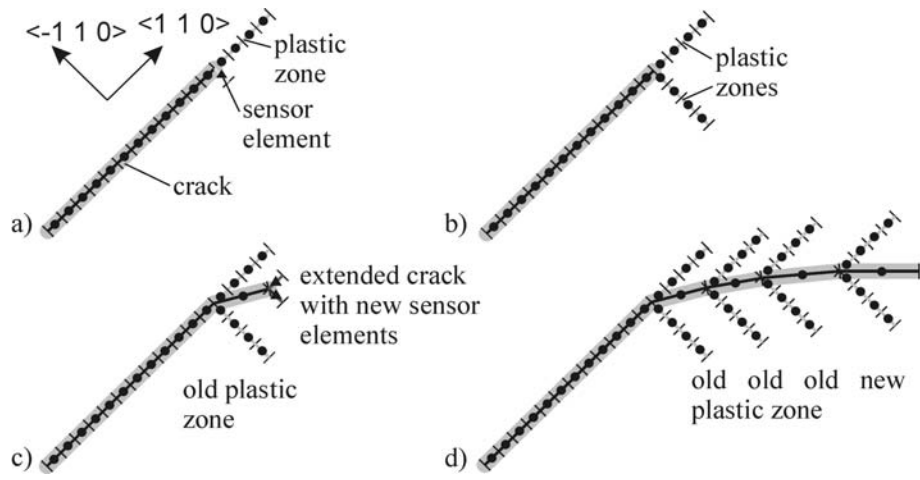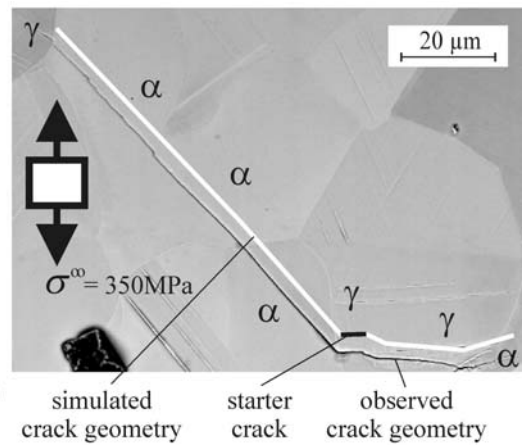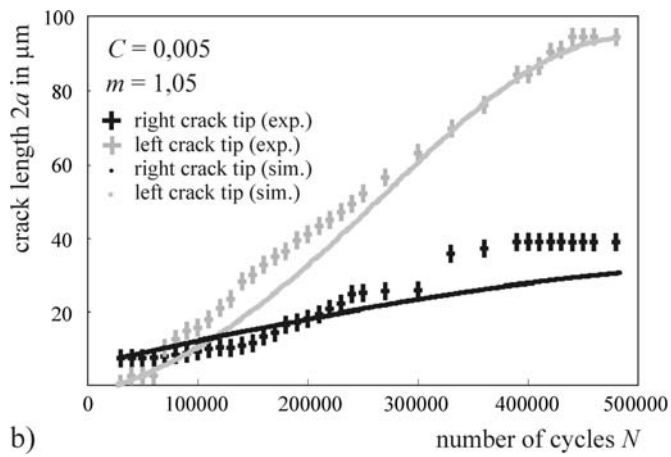
Fig. 11

Fig. 12

Figure Captions

Fig. 1: Schematic representation of the crack-propagation rate vs. crack length for long and short cracks interfering with microstructural barriers.

Fig. 2: Geometry of the shallow-notched specimens.

Fig. 3: Assembling new crack planes from slip planes

Fig. 4: Paths of short cracks a) $\Delta\sigma/2$=400 MPa, N=170,000; b) $\Delta\sigma/2$=370 MPa, N=160,000.

Fig. 5: Crack paths of two short cracks: (a) $\Delta\sigma/2$=370 MPa, N=160,000; (b) $\Delta\sigma/2$=350 MPa, N=1,100,000+5,000 overload cycles; (c) crack path in the bulk

Fig. 6: Hall-Petch plot of the results from the incremental step tests (IST).

Fig.7: Schematic representation of the short-crack model with boundary elements.

Fig. 8: Crack propagation across phase boundary.

Fig. 9: (a) Crack with sensor elements and (b) shear stress distribution around crack tip for a linear-elastic and a linear-elastic perfectly-plastic crack.

Fig. 10: Transition from single slip to multiple slip.

Fig. 11: Crack length versus number of cycles for two short cracks.

Fig. 12: Crack length versus number of cycles for a short crack growing by alternating operation of slip planes.